How to cite: *Angew. Chem. Int. Ed.* **2021**, *60*, 18065 – 18072
International Edition: doi.org/10.1002/anie.202102670
German Edition: doi.org/10.1002/ange.202102670

Metal–Organic Frameworks | Hot Paper

An Electrically Conducting Three-Dimensional Iron–Catecholate Porous Framework

Andre Mähringer[+], Markus Döblinger[+], Matthias Hennemann[+], Christoph Gruber, Dominik Fehn, Patricia I. Scheurle, Pouya Hosseini, Irina Santourian, Alfred Schirmacher, Julian M. Rotter, Gunther Wittstock, Karsten Meyer, Timothy Clark, Thomas Bein, and Dana D. Medina**

Abstract: *We report the synthesis of a unique cubic metal–organic framework (MOF), Fe-HHTP-MOF, comprising hexahydroxytriphenylene (HHTP) supertetrahedral units and Fe^{III} ions, arranged in a diamond topology. The MOF is synthesized under solvothermal conditions, yielding a highly crystalline, deep black powder, with crystallites of 300–500 nm size and tetrahedral morphology. Nitrogen sorption analysis indicates a highly porous material with a surface area exceeding 1400 $m^2 g^{-1}$. Furthermore, Fe-HHTP-MOF shows broadband absorption from 475 up to 1900 nm with excellent absorption capability of 98.5 % of the incoming light over the visible spectral region. Electrical conductivity measurements of pressed pellets reveal a high intrinsic electrical conductivity of up to 10^{-3} S cm^{-1}. Quantum mechanical calculations predict Fe-HHTP-MOF to be an efficient electron conductor, exhibiting continuous charge-carrier pathways throughout the structure.*

Introduction

In recent years, electrical conductivity has been added to the property portfolio of metal–organic framework (MOF) materials.[1] This exciting new feature in combination with the central properties of MOFs, including high crystallinity, porosity and enormous diversity of molecular building blocks, is expected to pave the way for new directions in fields such as charge storage, sensing and photovoltaic materials.[2,3] While thousands of crystalline, highly porous MOFs have been reported so far, only a small number of MOFs with moderate porosity have been found to be electrically conducting. Discovering framework materials that feature both high porosity and crystallinity combined with electrical conductivity remains a prodigious challenge. To date, electrically conducting MOFs are mainly 2D-layered structures, where charge migration occurs via both through-space and through-bond mechanisms.[4] The most prominent of these materials is the metal catecholate, M-CAT-1 series consisting of hexahydroxytriphenylene (HHTP) moieties and metal ions, such as Co^{II}, Ni^{II} or Cu^{II}.[5,6] This family of 2D-layered materials crystallizes in a hexagonal symmetry forming rod-like crystallites on the nanoscale that feature microporosity with Brunauer-Emmett-Teller (BET) surface areas reaching 350 $m^2 g^{-1}$. Four-point probe electrical conductivity measurements on Cu-CAT-1 single crystals revealed values of up to 0.1 S cm^{-1}. The family of layered catecholate-based MOFs was recently extended by employing the rare-earth metals La, Nd, Ho, and Yb in the synthesis. In this series, the lanthanide ions interconnect the planar ligands, forming a 3D framework through "out-of-plane" metal–oxo chains. By using rare-earth metals with different ionic radii, a fine-tuning of the stacking distances was achieved. This allowed for the control over charge-transport perpendicular to the sheets, with the re-

[*] Dr. A. Mähringer,[+] Dr. M. Döblinger,[+] M. Sc. C. Gruber, M. Sc. P. I. Scheurle, Dr. J. M. Rotter, Prof. T. Bein, Dr. D. D. Medina
Department of Chemistry
Ludwig-Maximilians-Universität (LMU)
& Center for NanoScience (CeNS)
Butenandtstrasse 11, 81377 Munich (Germany)
E-mail: bein@lmu.de
dana.medina@cup.lmu.de

Dr. P. Hosseini, Prof. G. Wittstock
School of Mathematics and Science
Department of Chemistry
Carl von Ossietzky University of Oldenburg
26111 Oldenburg (Germany)

M. Sc. I. Santourian, Dr. A. Schirmacher
Physikalisch-Technische Bundesanstalt (PTB) Braunschweig und Berlin
Bundesallee 100, 38116 Braunschweig (Germany)

M. Sc. D. Fehn, Prof. K. Meyer
Friedrich-Alexander-University Erlangen-Nürnberg (FAU)
Department of Chemistry & Pharmacy
Inorganic Chemistry
Egerlandstrasse 1, 91058 Erlangen (Germany)

Dr. M. Hennemann,[+] Prof. T. Clark
Friedrich-Alexander-University Erlangen-Nürnberg (FAU)
Computer-Chemistry-Center
Department of Chemistry & Pharmacy
Naegelsbachstrasse 25, 91052 Erlangen (Germany)

[+] These authors contributed equally to this work.

Supporting information and the ORCID identification number(s) for the author(s) of this article can be found under: https://doi.org/10.1002/anie.202102670.

ported electrical conductivity reaching 0.05 S cm^{-1}.[7] Exchanging the hydroxy functionalities of the triphenylene core with amino or thiol groups results in electron-rich building blocks, such as 2,3,6,7,10,11-triphenylenehexathiol (THT) or 2,3,6,7,10,11-hexaminotriphenylene (HATP). Diverse layered frameworks can be obtained by combining these building blocks with 3d transition metals to give high electrical conductivity or absorption shifted into the near IR region.[8] A prominent example is the π-conjugated $Fe_3(THT)_2(NH_4)_3$, which shows room-temperature charge-carrier mobility of up to 220 cm^2 V^{-1} s^{-1} and electrical conductivity values of 0.03 S cm^{-1}.[3,9] In contrast to their superior electronic properties, these materials feature relatively poor crystallinity and porosity, which is attributed to a rapid polymerization process owing to the high precursor reactivity. However, while electroactive 2D MOFs are well established, electroactive 3D MOFs are largely unknown.

Encoding high electrical conductivity in highly porous 3D structures presents an intriguing challenge. In such materials, charge carriers are expected to be exclusively transported through bonds in continuous hybrid molecular percolation channels due to the highly porous nature of the framework. In this context, cubic MOF structures are of particular interest where charge carriers percolate throughout the framework isotropically in contrast to π-stacked moieties, therefore eliminating the need for their alignment to efficiently transport (and potentially harvest) charge carriers. Examples of conducting 3D frameworks remain very rare in the literature and are mostly centered on mixed-valency iron MOFs.[10–12] For example, one strategy for implementing mixed valency in 3D frameworks was introduced by systematically changing the redox state of iron ions in the structure. Here, $K_xFe_2(BDP)_3$ ($0 \le x \le 2$; BDP^{2-} = 1,4-benzenedipyrazolate) was obtained by fractional reduction of $Fe_2(BDP)_3$ with potassium naphthalenide, resulting in a (two-point probe) conductivity increase from 3.5×10^{-7} S cm^{-1} to 0.025 S cm^{-1} measured for single crystals.[13] In another approach, iron ions in $Fe_2(BDT)_3$ (H_2BDT = 5,5′-(1,4-phenylene)bis(1*H*-tetrazole)) were oxidized upon exposure to ambient atmosphere to give a mixed-valence Fe^{II}/Fe^{III} framework with tunable single-crystal conductivity, ranging from 10^{-5} to 1 S cm^{-1}.[10] A different pathway for introducing mixed valency in 3D frameworks is the integration of redox-active organic building blocks. In this context, Long and co-workers introduced a cubic ferric semiquinoid MOF,[12] consisting of Fe^{III} and mixed-valence 2,5-dioxidobenzoquinones that exhibits a conductivity of 0.16 S cm^{-1}, however, no porosity was determined. In 2015, Yaghi and co-workers pioneered the 3D M-CAT family by synthesizing Fe-CAT-5, the first 3D catecholate-based frameworks that show ultrahigh proton conductivity (5.0×10^{-2} S cm^{-1}).[14] The structure of Fe-CAT-5 is built from iron and HHTP bridging units that form a 2-fold interpenetrating network with *srs* topology in which sulfate and dimethylammonium ions are part of the framework. Although these frameworks conduct protons well at higher relative humidity, their electrical conductivity remains unknown. Recently, Dinca and co-workers reported the synthesis of cubic faujasite-like, rare-earth-metal HHTP MOFs with intrinsic electrical conductivity values of up to 10^{-5} S cm^{-1}.[15] Nevertheless, to date, the combination of the transition metal iron with the well-known HHTP building unit to give a non-interpenetrating 3D catecholate-based framework with a defined structure, high porosity and high conductivity remains elusive.

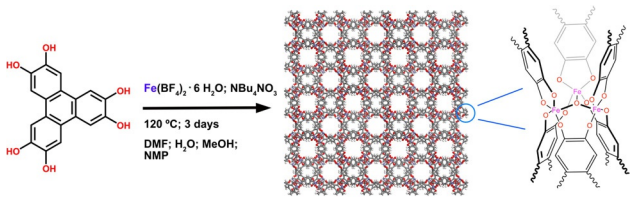

Figure 1. Synthesis scheme of 2,3,6,7,10,11-hexahydroxytriphenylene and an Fe^{II} precursor yielding the Fe-HHTP-MOF. The reaction was conducted under solvothermal synthesis conditions. Fe-HHTP-MOF shows a cubic porous structure with iron–oxo clusters (simplified model, for more information see Section "Structure Solution" in the SI) bridging the triphenylene building blocks.

We now present the synthesis of a novel metal–organic framework, coined Fe-HHTP-MOF, comprising the trigonal planar building block 2,3,6,7,10,11-hexahydroxytriphenylene and Fe^{III} ions (see Figure 1). Fe-HHTP-MOF features a pitch-black color and a ferric catecholate structure within a highly symmetric 3D cubic geometry with the space group *F*32, a result from combining powder X-ray diffraction (PXRD) data, transmission electron microscopy (TEM) analysis, energy-dispersive X-ray spectroscopy (EDX) and structural density functional theory (DFT) calculations. Furthermore, the microporous Fe-HHTP-MOF is highly porous with a BET surface area exceeding 1400 m^2 g^{-1}. Total hemispherical reflectance measurements of an Fe-HHTP-MOF pellet show a broad absorption, covering almost the entire UV/Vis and near-IR regions, yielding a total absorption of 98.5 % up to 800 nm. Van der Pauw measurements reveal high electrical conductivity values of up to 10^{-3} S cm^{-1}, among the highest conductivities reported for 3D MOFs to date. Zero-field ^{57}Fe Mössbauer, electron paramagnetic resonance (EPR) spectroscopy and superconducting quantum interference device (SQUID) magnetization analysis in combination with X-ray photoelectron spectroscopy (XPS) measurements were employed to study the iron valency in the framework. Quantum mechanical calculations show that Fe-HHTP-MOF is an efficient electron conductor but that it cannot transport holes because it exhibits no continuous paths for hole transport. These findings were obtained by means of direct semiempirical molecular-orbital molecular dynamics (MD) calculations. This intriguing combination of properties demonstrates that 3D frameworks can provide efficient through-bond charge-carrier migration pathways and, at the same time, remain highly porous and crystalline.

Results and Discussion

Synthesis Procedure. Fe-HHTP-MOF was synthesized under solvothermal reaction conditions. Briefly, $Fe(BF_4)_2 \cdot 6H_2O$ and 2,3,6,7,10,11-hexahydroxytriphenylene precursors were added to a solvent mixture of DMF

(dimethylformamide), MeOH (methanol), NMP (*N*-methyl-2-pyrrolidone), water, and tetrabutylammonium nitrate (NBu_4NO_3) crystallization additive under argon atmosphere (Figure 1). The reaction mixture was sealed under inert conditions and transferred to a preheated oven at 120 °C for 48 h. After the given reaction period, the reaction tube was retrieved and, upon cooling to room temperature, a dark black microcrystalline material was isolated and subsequently degassed under dynamic vacuum prior to analysis (for more details see SI).

Structure Solution. Powder X-ray diffraction (PXRD) patterns feature sharp reflections up to high 2θ values (20°, Figure 2 A), demonstrating the presence of a highly crystalline product. Scanning electron microscopy (SEM) analysis reveals tetrahedral and faceted intergrown crystallites, exhibiting edge-to-edge distances of 400 to 500 nm (Figure 2 E). Typically, the angles between facets of the tetrahedra observed were around 72°. TEM analysis shows crystalline domains, whose faces and lattice planes ($d = 19$ Å) enclose angles of around 71° (Figure 2 F, Table S1). These findings suggest a cubic crystal structure, whose {111} planes typically intersect at angles of 70.5°. Compositional analysis by TEM and SEM showed the presence of Fe, O and C, with residual amounts of nitrogen. In the absence of larger single crystals, further structural characterization was carried out by means of PXRD. In accordance with the above-mentioned observations, the MOF powder diffraction pattern can be fully indexed in the cubic crystal system with a lattice constant of $a = 32.92(\pm 0.01)$ Å using the X-cell program and the reflex module from Materials Studio 7.0.[16] The most prominent reflection of the diffraction pattern at 2.1° 2θ is the (111) reflection, whose *d*-spacing of 19.01 Å was observed by TEM as well. The structure was initially solved in the space group $F4_132$ by simulated annealing using the program package EXPO2014.[17] Subsequently, this structure model was subjected to force field geometry optimization and Rietveld refinement.[18] As different structural variants in the $F4_132$ space group lead to similarly good R_{wp}-values of around 2.5 %, the structure was optimized with DFT within the fixed lattice constraints, leading to a final structure model with space group *F*23 (Figure 2, see chapter "Structure Solution" in the SI).[19] The average composition determined by EDX spectroscopy (see Figure S2, Table S2), $C_{63.1}O_{29.0}Fe_{7.9}$, is close to the nominal refined composition of this structure model

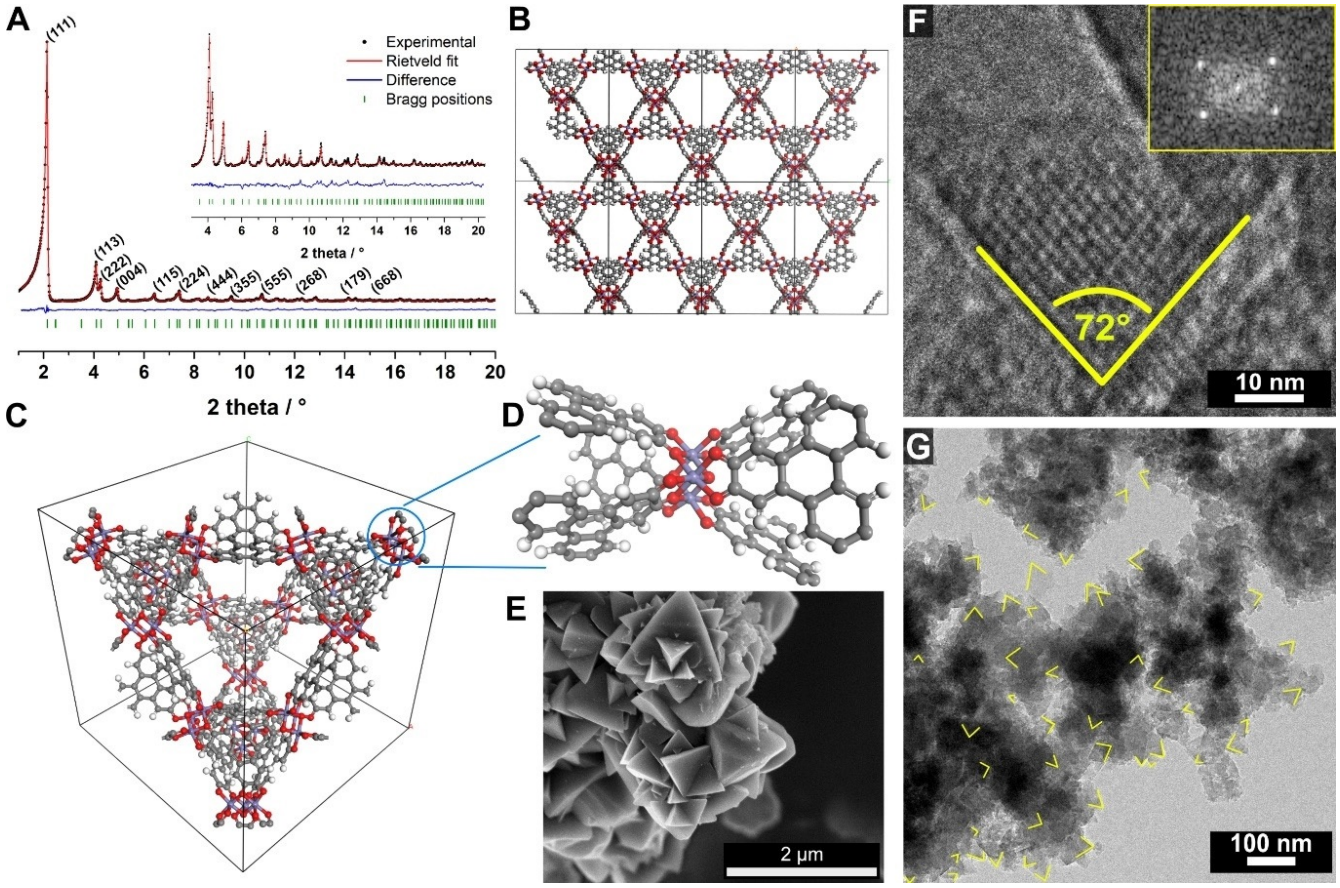

Figure 2. A) Mo-K_α source diffraction pattern of Fe-HHTP-MOF. B) View along the *c*-axis showing the tetrahedral arrangement of the HHTP ligands in the unit cell. C) View along the [111] direction visualizing the open pore system of the supertetrahedron comprised of bridging iron and HHTP molecules. D) Enlarged illustration of the central secondary building unit composed of three Fe ions in a trigonal arrangement, which are coordinated by a central oxygen and stabilized by a total of six HHTP ligands. E) SEM image showing tetrahedral intergrown crystallites with a size of 300–500 nm. F) TEM analysis depicts a tetrahedral crystallite. Inset: FFT from the crystal lattice of an exemplary crystallite agrees well with the lattice constant from the PXRD pattern. G) Crystalline domains in the sample showing a tetrahedral angle of 72°.

$C_{63.2}O_{31.4}Fe_{5.3}$ (without considering hydrogen). For more information, see the chapter "Structure Solution" in the SI.

Structure Description. In the structure model, each iron atom bridges two HHTP moieties. Three of these iron bis-catecholate complexes are arranged in a trimeric geometry, stabilized by a central oxygen atom (see Figure 2D), as observed in a number of other MOFs.[20] The oxo-trimers form the extended vertices of an open supertetrahedron, whose faces are the connecting HHTP moieties; each of them is linked to three iron oxo-trimers. The supertetrahedra are corner-connected to four other supertetrahedra, thus forming a porous 3D architecture. Considering a supertetrahedron to be the basic building unit, the structure can be described by a diamond (4-c dia) topology.[21] The smallest R_w-values were obtained for a structure model with water present in the pores.

Materials Characterization. Nitrogen ad- and desorption measurements revealed a type *Ia* isotherm according to the IUPAC nomenclature (Figure 3).[22] In the isotherms, the sharp uptake at relatively low partial pressure ($p/p_0 < 0.1$ and up to 350 $cm^3 g^{-1}$) points to a microporous structure. The desorption curve overlaps perfectly with the adsorption curve, indicating a highly reversible gas sorption process. The BET model was applied to the isotherms at low partial pressures ($p/p_0 < 0.1$) to give a BET surface area of 1490 $m^2 g^{-1}$, and a pore volume of 0.7 $cm^3 g^{-1}$. The measured BET surface area and pore volume agree well with the predicted Connolly surface area of 1675 $m^2 g^{-1}$ and pore volume of 1 $cm^3 g^{-1}$ calculated for the cubic model structure. The surface area of this cubic MOF is about four times higher than the average surface area for a corresponding 2D MOF, such as M-CAT-1.[6] In addition, the high surface area indicates that the pores of the MOFs are largely open, excluding the presence of large or sterically demanding reaction residues. The pore-size distribution was calculated by quenched solid density functional theory (QSDFT) calculations, which revealed one type of pores with a narrow pore size distribution and a mean pore size of 1.78 nm. This value is in good agreement with the predicted 2.0 nm pore size from the model structure. The thermal stability of Fe-HHTP-MOF was investigated by thermogravimetric analysis (TGA), showing structural integrity up to 185 °C. At this temperature, a mild weight loss occurs, associated with the slow degradation of the framework. At about 200 °C, a rapid combustion is observed that is attributed to the reaction of iron ions in the MOF forming thermodynamically stable products, such as iron oxides (Figure S5).

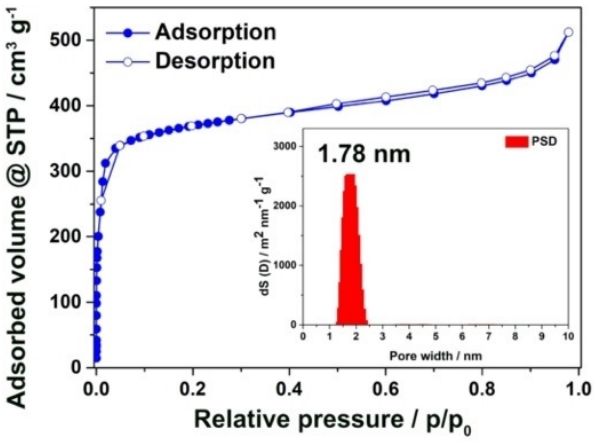

Figure 3. Nitrogen ad- and desorption isotherm. The inset shows the pore size distribution centered at 1.78 nm obtained by quenched solid density functional theory (QSDFT) calculations, revealing one type of pores and a narrow pore size distribution.

In addition to the EDX analysis, the composition and the presence of guest molecules in the MOF structure were further studied by X-ray photoelectron spectroscopy (XPS) experiments. To exclude the presence of impurities originating from the reaction precursors, such as $Fe(BF_4)_2 \cdot 6H_2O$, the boron spectrum was measured. Here, boron was not detected in the resulting spectrum (Figure S6). However, a weak nitrogen signal was identified and related to small amounts of residual DMF or tetrabutylammonium in the pores.

Photophysical Properties. The UV/Vis-NIR absorption spectrum of Fe-HHTP-MOF was measured in a diffuse reflectance geometry and constructed using the Kubelka–Munk equation (Figure 4). Fe-HHTP-MOF exhibits a broad absorption that covers large parts of the UV, visible and the near IR regions. The absorption spectrum shows local maxima at 380 nm and 950 nm, and the spectrum onset is located at 1400 nm in the near IR region. The TAUC equation

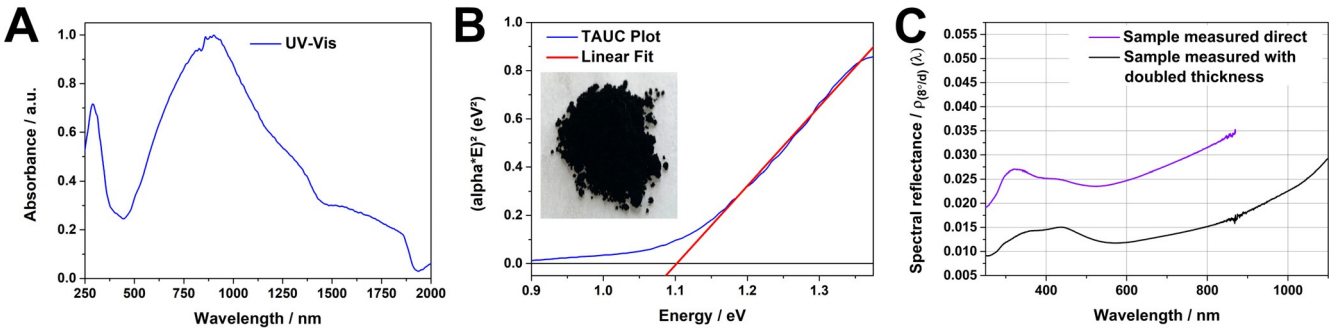

Figure 4. A) UV/Vis/NIR spectrum of Fe-HHTP-MOF showing a broad-band absorption ranging from 475 up to 1900 nm, giving the material a deep black appearance (inset in (B)). B) The material exhibits a direct band gap of 1.09 eV as indicated by the TAUC plot. C) Spectral reflectance measurements of pelletized samples with different thickness reveal low-reflection of not more than 0.015 over the whole visible spectrum up to 800 nm.

was employed to estimate the MOF band gap. Assuming a direct band gap and using the clear onset at 1400 nm, a band gap of 1.1 eV was determined. Powder photoluminescence measurements were conducted using a 375 nm laser source for excitation; however, no photoluminescence could be detected for the Fe-HHTP-MOF. Consistent with the broad-range absorption spectrum, Fe-HHTP-MOF appears as a pitch-black powder. Because of this, we conducted total hemispherical reflectance measurements to shed light on the quantitative reflection capabilities of the MOF material (Figure 4C). Here, the upper purple curve corresponds to a mechanically pressed sample of 3 mm thickness and the lower black curve corresponds to a sample with doubled thickness and a manual preparation of the sample surface. The Fe-MOF samples exhibit reflectance of less than 3% in the visible spectrum, regardless of the sample thickness. Strikingly, the highly porous and lightweight 3D MOF, hosting air in ordered cavities, features an absorption value of 98.5% over the whole UV/Vis/NIR region.

Iron Valency. To study the Fe valency in Fe-HHTP-MOF, ^{57}Fe Mössbauer analysis at 77 K was employed (Figure 5A). The zero-field spectrum shows one symmetric quadrupole doublet with an isomer shift, δ, of 0.54 mm s^{-1} and a quadrupole splitting, ΔE_Q, of 0.97 mm s^{-1}. This is in accordance with a single, high-spin Fe^{III} coordination site present in Fe-HHTP-MOF, and confirms the absence of residual Fe^{II} precursor material in the samples investigated. In addition, VT–VF SQUID magnetization studies on solid samples of Fe-HHTP-MOF, which reproducibly show temperature-dependent magnetic moments, μ_{eff}, with a value of circa 7.0 μ_B at 300 K, were obtained with applied fields of 0.01–7 T (Figure 5B). Upon cooling, μ_{eff} constantly decreases to reach 1.8 μ_B at 2 K (with 0.01 and 0.1 T, Figure S11). The magnetic data clearly suggest intramolecular, antiferromagnetic (AF) exchange interactions within the Fe_3-μ^3-oxo core of Fe-HHTP-MOF.[23,24] Various simulations (Figures S13–S15) advocate a "weakly spin-frustrated system" in an isosceles triangle of high-spin Fe^{3+} ions (d^5, $S_{Fe} = 5/2$) with two slightly different AF coupling constants (Figure S14, top). Notably, the detection of a "kink" in $\mu_{eff}(T) = 3.2$ μ_B at 7 K suggests thermal population of a low-lying quartet state, with contributions from a doublet state at base temperatures (Figure S14, bottom). The latter explains the slightly lower-than-spin-only value for an $S = 3/2$ state ($\mu_{eff}^{s.o.} = 3.83$ μ_B). It is quite remarkable to note that introduction of a "giant" diamagnetic contribution, well-established for graphite, for instance, results in a perfect simulation (Figure S15). Finally, continuous-wave (CW) X-band EPR spectra of the Fe-HHTP-MOF powder at 7, 95, and 293 K were recorded. At room temperature, the spectrum shows a single, broad and isotropic feature, centered at $g_{iso} = 2.02$ (Figure 5C, linewidth $W_{iso} = 120 \times 10^{-4}$ cm^{-1} GHz^{-1}). Notably, the line further broadens with decreasing temperature ($W_{iso} = 155 \times 10^{-4}$ cm^{-1} GHz^{-1} at 95 K and $W_{iso} = 315 \times 10^{-4}$ cm^{-1} GHz^{-1} at 7 K, Figure S9B,C). Considering that the magnetic results are dominated by the presence of a dense energy spectrum of close-lying magnetic states (see above), we presume that the peculiar spectral features result from fast relaxation between all accessible spin sub-levels of the spin-frustrated Fe^{III} trimeric units, which is mostly driven by weak "intermolecular" coupling of neighboring trimers. The intrinsic anisotropy of the zero-field splitting arising from multiple close-lying spin manifolds with $S > 1/2$ leads to the wide spread of magnetic resonances. These are centered around the electronic g values, because the effective g values for all Kramers doublets of any spin manifold, averaged over the unit sphere, concur in the electronic g value of the system, here $g_{iso} = 2.02$. Also, XPS data recorded for the same sample (Figure 5D) agree well with the results of the magnetochemical analysis. Here, the Fe 2p signal is split into two broad Fe 2p$_{3/2}$ and Fe 2p$_{1/2}$ peaks. Each peak was fitted by four components, which is in agreement with the reported interpretation of signals from high-spin

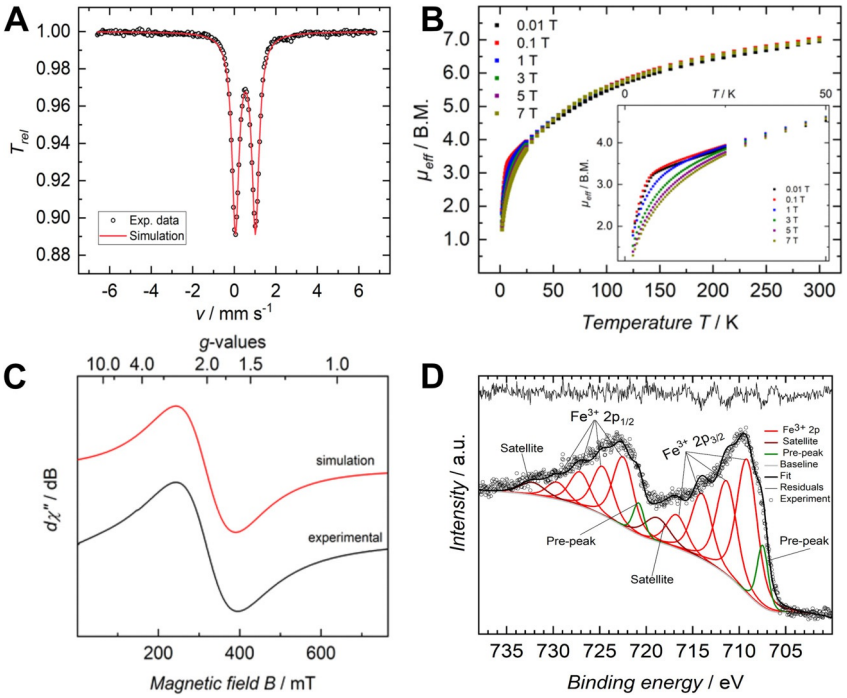

Figure 5. A) Zero-field ^{57}Fe Mössbauer spectrum of Fe-HHTP-MOF recorded at 77 K in the solid state. The Mössbauer spectrum shows one quadrupole doublet with an isomer shift, δ, of 0.54 mm s^{-1} and a quadrupole splitting parameter, ΔE_Q, of 0.97 mm s^{-1}. These parameters are in accordance with a high-spin Fe^{III} center. B) VT–VF SQUID measurements of a microcrystalline sample of Fe-HHTP-MOF, recorded with applied magnetic fields of 0.01 T (black square), 0.1 T (red squares), 1.0 T (blue squares), 3.0 T (green squares), 5.0 T (purple squares), and 7.0 T (yellow–green squares), plotted as μ_{eff} vs. T. The inset shows an enlargement of the low temperature region. The magnetic moments are given per trinuclear repeat unit. C) CW X-band EPR spectrum recorded with a microcrystalline sample at 293 K (experimental: black trace; simulation: red trace). D) XPS data of the Fe 2p region. The experimental data points are plotted as open circles, the envelope and residuals as solid black line, the multiplet components as red lines and the background as solid gray line.

Fe^{III}.[25] A single low-intensity peak (pre-peak) on the low-binding-energy (BE) side of the envelope was added to account for the potential formation of Fe ions with a lower oxidation state. To exclude structural defects derived from mixed-valance iron centers, the proportion Fe^{II} to Fe^{III} was estimated by comparing the area under the pre-peaks to the summed area of the other peak components. Considering the uncertainty margin in fitting, the ratio of these areal components is very far from any stoichiometric content. The appearance of Fe^{II} sites from reduction by secondary electrons during X-ray irradiation and the use of a flood gun for charge compensation is often observed in coordination network compounds. An XPS scan at the end of the measurement (Figure S6D) confirmed the absence of extensive radiation damage. Thus, we attribute the low intensity pre-peak observed to surface defects originating from a combination of sample handling and reduction by secondary electrons.

Electrical Conductivity. The electrical conductivity of Fe-HHTP-MOF was determined using both two-point-probe measurements and 4-point van der Pauw measurements with crystalline pellets of the material. The MOF pellet samples were prepared using 100 mg of the evacuated material and applying pressure of 45 $kg\,cm^{-2}$ using a standard KBr press (for further information see SI). SEM images of the pelletized sample confirm that the tetrahedral faceted crystallite morphology of the bulk material is preserved after compression (see Figure S3). The thickness of the pellets was measured by a slide gauge to be 500 µm. For two-point measurements, a linear sweep *I–V* scan was performed by applying voltage in the range of −1.5 to 1.5 V to give a linear ohmic resistance curve and electrical currents in the microampere range (Figure 6, S16). The curve was fitted by a linear regression and the slope of the linear function yielded an electrical conductivity of $1.1\times10^{-4}\,S\,cm^{-1}$. Further four-point probe van der Pauw measurements were conducted using the same pelletized samples to give an average electrical conductivity value of $5.6\times10^{-3}\,S\,cm^{-1}$ (Table S5). We note that the measurements of the pellets were conducted without applied pressure, hence, the current percolation pathways are expected to be limited by the grain-to-grain resistances. This implies that the intrinsic conductivity of the individual crystallites may be even much higher than $10^{-3}\,S\,cm^{-1}$.

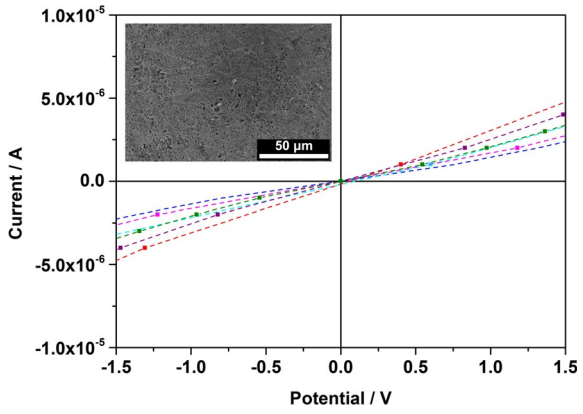

Figure 6. *I–V* curves of a pelletized Fe-HHTP-MOF sample measured via two-point probe showing an ohmic resistance and an electrical conductivity of $10^{-4}\,S\,cm^{-1}$.The different curves represent different spot locations on the sample surface, with dots for the data points and the dotted line as linear fit. The same sample showed an electrical conductivity of $10^{-3}\,S\,cm^{-1}$ with the four-probe analysis. The surface of the homogeneously compressed pellet is shown as an inset.

Charge-Carrier Pathway Simulations. Since Fe-HHTP-MOF is an electroactive material, we elucidated the possible charge-carrier migration pathways in the framework, using direct semiempirical molecular-orbital molecular-dynamics (MD) simulations and subsequent charge-propagation simulations. For the MD simulation, five picoseconds of PM6[26] direct semiempirical molecular-orbital MD on the periodic structure flooded with water (see SI for further details) were calculated, and a snapshot from the end of the simulation was used for imaginary-time-evolution simulations[27,28] of electron and hole transport. Details of all the simulations are given in the SI. The charge-transport simulations are based on the local average ionization energy[29] and the local electron affinity[30] for holes and electrons, respectively, and give the calculated conductance paths (Figure 7). The electron-transport path moves through the lattice via the iron centers and the connecting ligands. The path is continuous, indicating polaron transport along conducting chains of atoms. This result can be rationalized by considering both the iron centers Fe^{II}/Fe^{III} and the catechol moieties (semiquinone/catechol) to be redox active.[31] Here, the ligands can provide reducible paths for transporting electrons between iron centers. This mechanism will be described in more detail in a later study. In contrast, the hole-transport path is discontinuous with local charge centers largely located on the water clusters used to flood the MOF. This indicates hopping conductance between water basins with little involvement of the MOF framework. Although imaginary time propagation cannot give quantitative mobilities,[27,28] we note that the electron moves essentially twice as far as the hole in the two equivalent simulations shown above. These results are expected from the local ionization energy and local electron affinity maps (Figure 7C,D). The local electron affinity isodensity surface plotted at a value of 0 $kcal\,mol^{-1}$ shows an almost continuous envelope around the MOF framework, indicating that electrons can move relatively freely (Figure 7C). In contrast, the local ionization energy isosurface (depicted at 330 kcal mol^{-1}) shows isolated islands with no continuous easily ionizable path through the network (Figure 7D). This leads to the hopping conductance between water clusters shown in Figure 7A. Thus, the simulations suggest that Fe-HHTP-MOF is an efficient electron conductor but that it cannot transport holes because it exhibits no continuous paths for hole transport through the MOF framework and because its ionization potential is high. The local electron affinity, on the other hand, shows continuous bound transport paths along the framework of the MOF.

Conclusion

Herein, we present the synthesis of a cubic ferric catecholate framework material coined Fe-HHTP-MOF. The Fe-HHTP-MOF is obtained in a solvothermal reaction

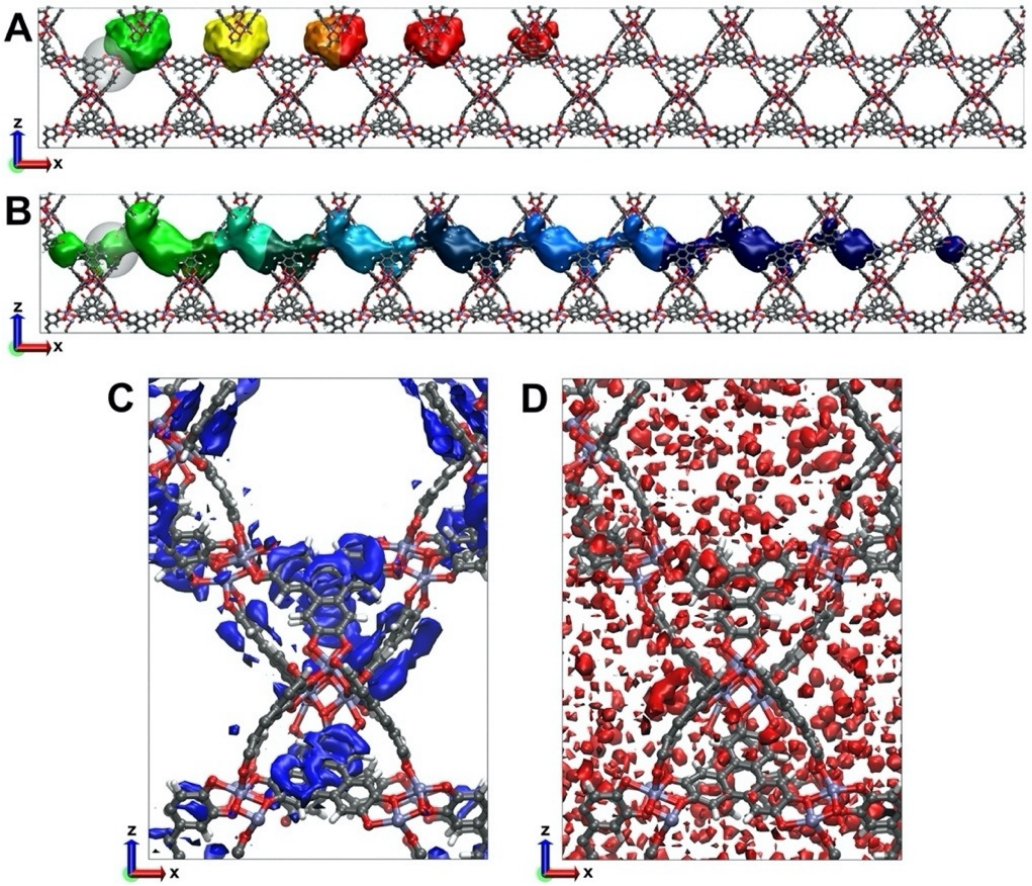

Figure 7. A) Calculated hole- and B) electron-transport paths. Isocontour plots for 8 time steps (24 fs each) of the electron (green to blue) and hole density (green to red; contour level = 1.2×10^{-5} e-Bohr^{-3}). The initial Gaussian function is shown as transparent sphere. Isocontour plots of C) the PM6 local electron affinity (contour level = 0 kcal mol^{-1}) and D) local ionization energy (contour level = 330 kcal mol^{-1} = 14.3 eV).

as a dark black powder consisting of intergrown tetrahedral crystallites in the 300–500 nm size range. The structure was solved from powder X-ray diffraction data using a Mo-K_α source by indexing and a subsequent simulated annealing step. The unit cell obtained was subjected to a DFT optimization and Rietveld refinement to give a final structure model with the cubic space group *F*23. The structure of Fe-HHTP-MOF is composed of iron-connected supertetrahedra to give a diamond-like topology. The tetrahedra are composed of four triphenylene units that form the facets and are interconnected by a defined trinuclear iron–oxo cluster. The Fe-HHTP-MOF is microporous with a BET surface area exceeding 1400 m^2 g^{-1}. Moreover, Fe-HHTP-MOF combines this high surface area with electrical conductivity of about 10^{-3} S cm^{-1}, thus establishing an exceptionally high intrinsic conductivity for a 3D-connected framework. The deep black appearance of the material was studied by reflectance measurements, giving a remarkably low degree of reflection up to 1.5% in the visible spectral regime for a porous framework. The nature of the ferric repeat unit was elucidated by means of XPS, EPR, SQUID, and ^{57}Fe Mössbauer measurements, indicating the presence of a purely ferric, high-spin Fe^{III} framework. To gain further insights into the electrical conductivity of Fe-HHTP-MOF, we performed quantum mechanical calculations, which suggest the Fe-HHTP-MOF to be an efficient electron conductor that exhibits continuous paths through the conducting framework atoms. This work sheds light on the subtle interplay of the structure, porosity, electronic properties, electrical conductance, and broad-band optical absorption of novel framework materials, which serves as a blueprint for the future design of electrically conducting metal–organic frameworks. The combination of the substantial porosity of Fe-HHTP-MOF with high electrical conductivity and a narrow direct band gap offers exciting opportunities for the design of novel chemical sensors, organic optoelectronics, and for electric control of mass transport in porous systems, such as microfluidics.

Acknowledgements

The authors are grateful for financial support from the Deutsche Forschungsgemeinschaft (DFG) in the context of the National Research Network COORNETs (SPP 1928), the Excellence Clusters "Nanosystems Initiative Munich (NIM)" and "e-conversion" (the latter funded under Germany's Excellence Strategy—EXC 2089/1-390776260), and from the Free State of Bavaria through the Research Network "Solar Technologies go Hybrid". D.F. and K.M. acknowledge generous funding from FAU and thank Dr. Eckhard Bill (MPI

CEC) for insightful discussions regarding the material's magnetochemical properties. Open access funding enabled and organized by Projekt DEAL.

Conflict of interest

The authors declare no conflict of interest.

Keywords: electrical conductivity · iron-catecholate · metal–organic frameworks · porosity · three-dimensional framework

[1] a) L. Sun, M. G. Campbell, M. Dincă, *Angew. Chem. Int. Ed.* **2016**, *55*, 3566; *Angew. Chem.* **2016**, *128*, 3628; b) L. S. Xie, G. Skorupskii, M. Dincă, *Chem. Rev.* **2020**, *120*, 8536 – 8580; c) D. D. Medina, A. Mähringer, T. Bein, *Isr. J. Chem.* **2018**, *58*, 1089.

[2] a) M. G. Campbell, S. F. Liu, T. M. Swager, M. Dincă, *J. Am. Chem. Soc.* **2015**, *137*, 13780; b) D. Feng, T. Lei, M. R. Lukatskaya, J. Park, Z. Huang, M. Lee, L. Shaw, S. Chen, A. A. Yakovenko, A. Kulkarni, et al., *Nat. Energy* **2018**, *3*, 30; c) A. Mähringer, A. C. Jakowetz, J. M. Rotter, B. J. Bohn, J. K. Stolarczyk, J. Feldmann, T. Bein, D. D. Medina, *ACS Nano* **2019**, *13*, 6711; d) P. I. Scheurle, A. Mähringer, A. C. Jakowetz, P. Hosseini, A. F. Richter, G. Wittstock, D. D. Medina, T. Bein, *Nanoscale* **2019**, *11*, 20949.

[3] H. Arora, R. Dong, T. Venanzi, J. Zscharschuch, H. Schneider, M. Helm, X. Feng, E. Cánovas, A. Erbe, *Adv. Mater.* **2020**, *32*, 1907063.

[4] a) L. S. Xie, E. V. Alexandrov, G. Skorupskii, D. M. Proserpio, M. Dincă, *Chem. Sci.* **2019**, *10*, 8558; b) H. Jia, Y. Yao, J. Zhao, Y. Gao, Z. Luo, P. Du, *J. Mater. Chem. A* **2018**, *6*, 1188; c) X. Huang, P. Sheng, Z. Tu, F. Zhang, J. Wang, H. Geng, Y. Zou, C.-a. Di, Y. Yi, Y. Sun et al., *Nat. Commun.* **2015**, *6*, 7408.

[5] R. W. Day, D. K. Bediako, M. Rezaee, L. R. Parent, G. Skorupskii, M. Q. Arguilla, C. H. Hendon, I. Stassen, N. C. Gianneschi, P. Kim, et al., *ACS Cent. Sci.* **2019**, *5*, 1959.

[6] M. Hmadeh, Z. Lu, Z. Liu, F. Gándara, H. Furukawa, S. Wan, V. Augustyn, R. Chang, L. Liao, F. Zhou, et al., *Chem. Mater.* **2012**, *24*, 3511.

[7] G. Skorupskii, B. A. Trump, T. W. Kasel, C. M. Brown, C. H. Hendon, M. Dincă, *Nat. Chem.* **2020**, *12*, 131.

[8] a) R. Dong, Z. Zheng, D. C. Tranca, J. Zhang, N. Chandrasekhar, S. Liu, X. Zhuang, G. Seifert, X. Feng, *Chem. Eur. J.* **2017**, *23*, 2255; b) J.-H. Dou, L. Sun, Y. Ge, W. Li, C. H. Hendon, J. Li, S. Gul, J. Yano, E. A. Stach, M. Dincă, *J. Am. Chem. Soc.* **2017**, *139*, 13608; c) D. Sheberla, L. Sun, M. A. Blood-Forsythe, S. Er, C. R. Wade, C. K. Brozek, A. Aspuru-Guzik, M. Dincă, *J. Am. Chem. Soc.* **2014**, *136*, 8859; d) Z. Jin, J. Yan, X. Huang, W. Xu, S. Yang, D. Zhu, J. Wang, *Nano Energy* **2017**, *40*, 376.

[9] R. Dong, P. Han, H. Arora, M. Ballabio, M. Karakus, Z. Zhang, C. Shekhar, P. Adler, P. S. Petkov, A. Erbe, et al., *Nat. Mater.* **2018**, *17*, 1027.

[10] L. S. Xie, L. Sun, R. Wan, S. S. Park, J. A. DeGayner, C. H. Hendon, M. Dincă, *J. Am. Chem. Soc.* **2018**, *140*, 7411.

[11] J. G. Park, M. L. Aubrey, J. Oktawiec, K. Chakarawet, L. E. Darago, F. Grandjean, G. J. Long, J. R. Long, *J. Am. Chem. Soc.* **2018**, *140*, 8526.

[12] L. E. Darago, M. L. Aubrey, C. J. Yu, M. I. Gonzalez, J. R. Long, *J. Am. Chem. Soc.* **2015**, *137*, 15703.

[13] M. L. Aubrey, B. M. Wiers, S. C. Andrews, T. Sakurai, S. E. Reyes-Lillo, S. M. Hamed, C.-J. Yu, L. E. Darago, J. A. Mason, J.-O. Baeg, et al., *Nat. Mater.* **2018**, *17*, 625.

[14] N. T. T. Nguyen, H. Furukawa, F. Gándara, C. A. Trickett, H. M. Jeong, K. E. Cordova, O. M. Yaghi, *J. Am. Chem. Soc.* **2015**, *137*, 15394.

[15] G. Skorupskii, M. Dincă, *J. Am. Chem. Soc.* **2020**, *142*, 6920.

[16] M. Neumann, *J. Appl. Crystallogr.* **2003**, *36*, 356.

[17] a) A. Altomare, N. Corriero, C. Cuocci, A. Falcicchio, A. Moliterni, R. Rizzi, *J. Appl. Crystallogr.* **2018**, *51*, 505; b) A. Altomare, N. Corriero, C. Cuocci, A. Moliterni, R. Rizzi, *J. Appl. Crystallogr.* **2013**, *46*, 779.

[18] a) A. K. Rappe, C. J. Casewit, K. S. Colwell, W. A. Goddard, W. M. Skiff, *J. Am. Chem. Soc.* **1992**, *114*, 10024; b) R. A. Young, *The Rietveld Method*, Oxford University Press, Oxford, **1995**.

[19] Deposition Number 2069404 contains the supplementary crystallographic data for this paper. These data are provided free of charge by the joint Cambridge Crystallographic Data Centre and Fachinformationszentrum Karlsruhe Access Structures service www.ccdc.cam.ac.uk/structures.

[20] O. I. Lebedev, F. Millange, C. Serre, G. van Tendeloo, G. Férey, *Chem. Mater.* **2005**, *17*, 6525.

[21] a) W. Bragg, *Nature* **1913**, *91*, 557; b) D. Kim, X. Liu, M. S. Lah, *Inorg. Chem. Front.* **2015**, *2*, 336; c) M. Li, D. Li, M. O'Keeffe, O. M. Yaghi, *Chem. Rev.* **2014**, *114*, 1343.

[22] M. Thommes, K. Kaneko, A. V. Neimark, J. P. Olivier, F. Rodriguez-Reinoso, J. Rouquerol, K. S. W. Sing, *Pure Appl. Chem.* **2015**, *87*, 1051.

[23] S. M. Gorun, G. C. Papaefthymiou, R. B. Frankel, S. J. Lippard, *J. Am. Chem. Soc.* **1987**, *109*, 4244.

[24] A. K. Boudalis, Y. Sanakis, F. Dahan, M. Hendrich, J.-P. Tuchagues, *Inorg. Chem.* **2006**, *45*, 443.

[25] a) R. P. Gupta, S. K. Sen, *Phys. Rev. B* **1974**, *10*, 70; b) R. P. Gupta, S. K. Sen, *Phys. Rev. B* **1975**, *12*, 15; c) A. P. Grosvenor, B. A. Kobe, M. C. Biesinger, N. S. McIntyre, *Surf. Interface Anal.* **2004**, *36*, 1564.

[26] J. J. P. Stewart, *J. Mol. Model.* **2007**, *13*, 1173.

[27] M. Kriebel, M. Hennemann, F. R. Beierlein, D. D. Medina, T. Bein, T. Clark, *J. Chem. Inf. Model.* **2019**, *59*, 5057.

[28] M. Kriebel, D. Sharapa, T. Clark, *J. Chem. Theory Comput.* **2017**, *13*, 6308.

[29] P. Sjoberg, J. S. Murray, T. Brinck, P. Politzer, *Can. J. Chem.* **1990**, *68*, 1440.

[30] a) T. Clark, *J. Mol. Model.* **2010**, *16*, 1231; b) B. Ehresmann, M. J. de Groot, A. Alex, T. Clark, *J. Chem. Inf. Comput. Sci.* **2004**, *44*, 658.

[31] B. Kalyanaraman, C. C. Felix, R. C. Sealy, *Environ. Health Perspect.* **1985**, *64*, 185.

Manuscript received: February 22, 2021
Revised manuscript received: March 11, 2021
Accepted manuscript online: March 29, 2021
Version of record online: July 1, 2021

